Multifractal evaluation of simulated precipitation intensities from the COSMO NWP model

Daniel Wolfensberger[1], Auguste Gires[2], Ioulia Tchiguirinskaia[2], Daniel Schertzer[2], and Alexis Berne[1]

[1]LTE, Ecole polytechnique fédérale de Lausanne (EPFL), Lausanne, Switzerland
[2]HMCO, Ecole des Ponts, UPE, Champs-sur-Marne, France

Correspondence to: Daniel Wolfensberger (daniel.wolfensberger@epfl.ch)

Abstract. The framework of universal multifractals (UM) allows to characterize the spatio-temporal variability of geophysical data over a wide range of scales with only a limited number of scale-invariant parameters. This work aims at clarifying the link between multifractals and more conventional weather descriptors and to show how they can be used to perform a multi-scale evaluation of model data.

The first part of this work focuses on a climatological study of precipitation intensities simulated by the COSMO numerical weather prediction model using the UM framework. Analysis of the spatial structure of the multifractal parameters and their correlations with external meteorological and topographic descriptors reveals that simulated precipitation tends to be smoother at higher altitudes and that the mean intermittency is mostly influenced by the latitude. A hierarchical clustering was performed on the external descriptors yielding three different classes, which correspond roughly to Alpine, Mediterranean and temperate/continental regions. Distributions of multifractal parameters within these three classes are shown to be statistically significantly different, indicating that the multifractal signature of rain is indeed climate dependent.

The second part of this work is event based and focuses on the smaller scales: the multifractal parameters of precipitation intensities at the ground are compared with those obtained from the Swiss radar composite during three events corresponding to typical synoptic conditions over Switzerland. The results of the analysis show that the COSMO simulations exhibit spatial scaling breaks that are not present in the radar data, indicating that the model is not able to simulate the observed variability at all scales. Comparison of the standard operational one-moment microphysical scheme with a more advanced two-moments scheme shows that while no scheme outperforms systematically the other, the two-moment scheme tends to produce larger extreme values which agree better with the radar composite.

1 Introduction

Validation of precipitation fields simulated by a numerical weather prediction model is a delicate task as reference data (rain gauges, radar scans) are typically available at a different spatial and temporal resolution than the model.

Traditional point-based verification scores are generally unable to provide sufficient information about the forecast quality as they do not consider the spatial structure of the data and are affected by the so-called "double penalty" (Gilleland et al., 2009). Indeed, small displacements in the simulated forecast features will be penalized twice, once for missing the observation and again for giving a false alarm. The impact of this double penalty is related to the variability of the simulated fields, which tends to increase with the resolution of the model. Numerous methods have been proposed in recent years to address this issue. Some methods rely on the use of traditional scores but applied on filtered fields, estimating the forecast performance as a function of scale and precipitation intensity (e.g., Ebert, 2008; Mittermaier et al., 2013) while others detect specific features on forecast and verification fields and compare these features based on their attributes (e.g., Davis et al., 2006; Wernli et al., 2008). Some other methods rely on the separation of scales with the use of space-frequency tools such as the 2D wavelet transform (Vasić et al., 2007).

Multifractals (MF) offer a convenient way to analyze the variability of complex geophysical systems globally over a wide range of scales. In the context of multifractals, the statistical properties of a field are related to the resolution by a power-law (Schertzer and Lovejoy, 1987). Universal Multifractals (UM) are a framework based on the concept of multiplicative cascades, which allows to analyse and simulate a high variability across scales with only a small number of parameters with physical meaning (e.g., Schertzer and Lovejoy, 1987; Lovejoy and Schertzer, 2007). In meteorology, UM have been used to study a large variety of complex natural phenomena such as the distribution of rainfall intensities at the ground (e.g., Marsan et al., 1996; Gires et al., 2015a, b), atmospheric turbulence (e.g., Parisi and Frisch, 1985a; Schertzer and Lovejoy, 2011) or climate change (e.g., Schmitt et al., 1995; Royer et al., 2008).

Gires et al. (2011), used the UM framework to compare simulations of Meso-NH, a non-hydrostatic numerical weather prediction (NWP) model developed by Météo-France, with composite radar images during a heavy convective rainfall event. This comparison showed that both the radar quantitative precipitation estimation (QPE) and the model simulations were generally characterized by similar ranges of scaling and agreed quite well with a simple space-time scaling model.

Gires et al. (2011)'s work focused on a rather flat area and a single event. It is therefore relevant to study multifractal behavior of model simulations and radar observations over a more complex terrain in a broader synoptic context. This work is thus divided in two parts. The first part aims to illustrate the use of multifractals for characterizing regional patterns of precipitation and to relate multifractals to synoptic and topographic features. To this end a large scale analysis of five years of simulated precipitation intensities from the COSMO numerical weather prediction model is conducted. The multifractal properties of the corresponding climatology of precipitation intensities are then studied and related to several regional and synoptic descriptors. The second part of this paper extends the work of Gires et al. (2011) over Switzerland for three different synoptic situations (snowstorm, stratiform rainfall and convective summer precipitation) by using simulations of precipitation intensities from the COSMO model run with different microphysical parameterizations.

This article is structured as follows: in section 2 the COSMO model as well as the Swiss radar composite are briefly described. The studied events as well as the radar data sets and model variables are then described in details, followed by a summary of the UM framework. In section 3, a climatological analysis of precipitation intensities simulated by COSMO is performed using the UM framework, in link with external geographic and meteorological descriptors. In section 4, a spatial and temporal analysis of precipitation intensities on the ground simulated by COSMO is performed during three characteristic events. The results are then compared with the UM analysis of the radar composite. Finally section 5 gives a summary of the main results and concludes this work.

2   Description of the data

2.1   The COSMO model

The COSMO model is a mesoscale limited area numerical weather prediction model initially developed as the Lokal Modell (LM) at the Deutscher Wetterdienst (DWD). It is now operated and developed by various weather services in Europe, including Switzerland. Besides its operational applications it is also used for scientific purposes in weather prediction and for regional climate simulations. The COSMO model is a non-hydrostatic model based on the fully compressible primitive equations integrated using a split-explicit third-order Runge–Kutta scheme (Wicker and Skamarock, 2002). The spatial discretization is based on a fifth-order upstream advection scheme on an Arakawa C-grid with Lorenz vertical staggering. Height-based Gal-Chen coordinates are used in the vertical (Gal-Chen and Somerville, 1975). In the horizontal the model uses a rotated coordinate system where the pole is displaced to ensure approximatively horizontal resolution over the model domain. Sub-grid scale processes are taken into account with parameterizations. In particular grid-scale clouds and precipitation are parameterized operationally with a one-moment scheme similar to Rudledge and Hobbs (1983) and Lin et al. (1983) with five hydrometeor categories: rain, snow, graupel, ice crystals and cloud droplets. Snow is assumed to be in the form of rimed aggregates of ice-crystals that have become large enough to have an appreciable fall velocity. Cloud ice is assumed to be in the form of small hexagonal plates that are suspended in the air and have no appreciable fall velocity. The particle size distributions (PSD) are assumed to be exponential for all hydrometeors, except for rain where a gamma PSD is assumed:

$$N(D) = N_0 D^{\mu} \exp(-\Lambda \cdot D) \quad \mathrm{m}^{-3}\mathrm{mm}^{-1} \tag{1}$$

where D is the equivolume diameter, N_0 is the intercept parameter ($\mathrm{m}^{-3}\mathrm{mm}^{-1}$), Λ the slope parameter (mm^{-1}) and μ the dimensionless shape parameter

In the one-moment scheme, which is used operationally, the only free parameter of the PSDs is the slope parameter Λ which can be obtained from the prognostic moment of order three (mass concentrations). The intercept parameter N_0 is either assumed to be constant or in the case of snow to be temperature dependent. The scale parameter μ is

3

equal to zero (exponential PSDs) for all hydrometeors except for rain where it is set to 0.5 by default. Mass-diameter relations as well as velocity-diameter relations for the precipitating hydrometeors are assumed to be power-laws.

A more advanced two-moments scheme with hail as a sixth hydrometeor category, was developed for COSMO by Seifert and Beheng (2006). In this scheme all PSDs are assumed to be gamma distributions where the intercept and slope parameters are free parameters that can be obtained from the prognostic moments of order zero (number concentrations) and order three (mass concentrations). As this scheme significantly increases the overall computation time it is currently not used operationally.

In COSMO, the interaction of various microphysical processes and their feedback on the simulated flow fields are represented by a system of budget equations for q^x, the specific mass fraction in kg_x per kg_{air} for hydrometeor x.

$$\frac{\partial q^x}{\partial t} + \mathbf{v} \cdot \nabla q^x - \frac{1}{\rho}\frac{\partial P^x}{\partial z} = S^x - \frac{1}{\rho}\nabla \cdot \mathbf{F}^x \tag{2}$$

where S^x represent the microphysical sources and sink per unit mass of moist air, $\mathbf{F}^x$ are the turbulent fluxes and P^x denotes the precipitation or sedimentation fluxes defined by $P^x = \rho q^x v_T^x$, where $v_T^{(j)}$ is the terminal fall velocity of hydrometeor j. The precipitation intensity at the ground is then simply the sum of the sedimentation fluxes of all hydrometeors at the lowest model level. In terms of terminal velocities COSMO assumes power-laws $v_T = aD^b$, where D is the particle equivolume diameter, for all hydrometeor types except for rain in the two-moment scheme, where an empirical relation by Rogers et al. (1993) is used.

Numerically this system of differential equations is treated with a time splitting method, in which the advection terms $\mathbf{v} \cdot \nabla q^x$ are first integrated over a COSMO time step (20 sec) and the budget equations are then solved for the microphysical source terms and sedimentation only. In the operational microphysical scheme the source terms include (1) *nucleation and depositional growth of cloud ice*, (2) *autoconversion of cloud water to rain*, (3) *collection mechanisms*, (4) *diffusional growth of rain and snow* and (5) *melting and freezing mechanisms.* Details about the parameterization of all these source terms can be found in Doms et al. (2011).

In the operational set-up, the COSMO model uses a prognostic turbulent kinetic energy (TKE) closure at level 2.5 for the parametrization of atmospheric turbulence. This scheme is similar to Mellor and Yamada (1982), the main difference being the use of variables that are conserved under moist adiabatic processes: total cloud water and liquid water potential temperature. Additionally, a so-called "circulation term" is included which describes the transfer of non-turbulent sub-grid kinetic energy from larger-scale circulation toward TKE. The reader is referred to Baldauf et al. (2011) and the model documentation (Doms et al., 2011) for a more in-depth description of the various COSMO sub-grid parameterizations.

2.2 Climatological study

In the first part of this work a multifractal characterization of all precipitation intensities simulated by COSMO during five years is performed. The computed multifractal parameters are then related to various descriptors. A

4

Name	Description	Unit
Average altitude	average altitude	m
Midpoint latitude	latitude of the square center	degree north
Midpoint longitude	longitude of the square center	degree east
Total precipitation	Total precipitation during all years	mm
Standard deviation of precipitation	Average standard deviation during timesteps with precip.	mm
Wet fraction	Fraction of simulated precipitation amounts that exceed a threshold of 0.1 mm per hour	-
Geopotential	average geopotential height at 850 hPa	m
Wind magnitude	average magnitude of the wind at 850 hPa	ms^{-1}
Wind direction	average wind direction at 850 hPa	degree
Temperature	average temperature at 850 hPa	K
Potential vorticity	average potential vorticity at 850 hPa	$\mathrm{m}^2 \ \mathrm{kg}^{-1} \ \mathrm{s}^{-1}$

Table 1. Short description of the three considered precipitation events

total of 43115 hourly timesteps of COSMO simulations in analysis mode covering a period of 5 years (2011 to 2016) were retrieved from the MeteoSwiss archives. This data is available at a 2 km resolution (0.02° angular resolution) using a set-up known operationally as "COSMO-2" (COSMO, 2015), which was used for operational forecast and analysis until beginning of 2016. The first and last 100 kilometers of the COSMO-2 domain along both longitudinal and latitudinal directions were discarded from the analysis in order to avoid border effects. The remaining area is shown in Figure 2 (Domain 1). This area was then divided into 209 sub-squares of size 64x64 (128x128 km^2), with an overlap of 2/3 between consecutive squares. This ratio has been chosen as a trade-off between representativity (total number of squares) and computation time.

Besides the multifractal parameters, which will be described later on, 11 local descriptors of the geography and meteorology were computed from the COSMO data within every square (Table 1).

Day	Timeline	Number of time steps	Description
26 March 2010	08:00 - 18:00	144 (12 h)	Crossing of a strong cold front causing sudden drop of temperature followed by heavy graupel and snowfall as well as strong winds
8 April 2014	02:00 - 10:00	144 (12 h)	Stationary front with widespread stratiform precipitation over Switzerland
13 August 2015	12:00 - 24:00	144 (12 h)	Strong summer convection triggered by the presence of very warm and wet subtropical air over Switzerland

Table 2. Short description of the three considered precipitation events

2.3 QPE comparison

2.3.1 Simulation of events

In the second part of this work, three precipitation events were simulated with COSMO and compared to the radar QPE in terms of the multifractal properties of their rainfall intensity fields. These events correspond to three typical synoptic situations observed over Switzerland. A brief description of the events is given in Table 2 and 500 hPa geopotential and temperature charts are shown in Figure 1. To simulate these events, COSMO was used in its version 5.01 with the standard "COSMO-2" set-up (COSMO, 2015). As was done in similar studies (Bohme et al., 2009), a spin-up time of 12 hours was used to account for the cold start of the model. For the initial and boundary conditions, analysis forcings of MeteoSwiss obtained with the COSMO-7 model run at 7 km resolution were used in order to run the model in analysis mode by correcting it with the most accurate information available at the time of simulation. In addition, the events were also simulated using the non-operational two-moment scheme, while keeping all other namelist parameters unchanged. For all simulations, model outputs were written every 5 minutes of simulated time, which corresponds to the temporal resolution of the Swiss radar composite.

2.3.2 QPE data

2.4

Precipitation intensities at the ground simulated by the COSMO model were compared with the quantitative precipitation estimation (QPE) product from the Swiss operational radar composite. The Swiss radar composite consists of the plane position indicator (PPI) measurements of the four [1] operational polarimetric C-band radars. The QPE product of MeteoSwiss is computed in the following way. The linear equivalent radar reflectivity measurement at up to six $1° \times 1° \times 83$m clutter-free radar bins, corrected for partial beam-blocking, are averaged to derive polar

---

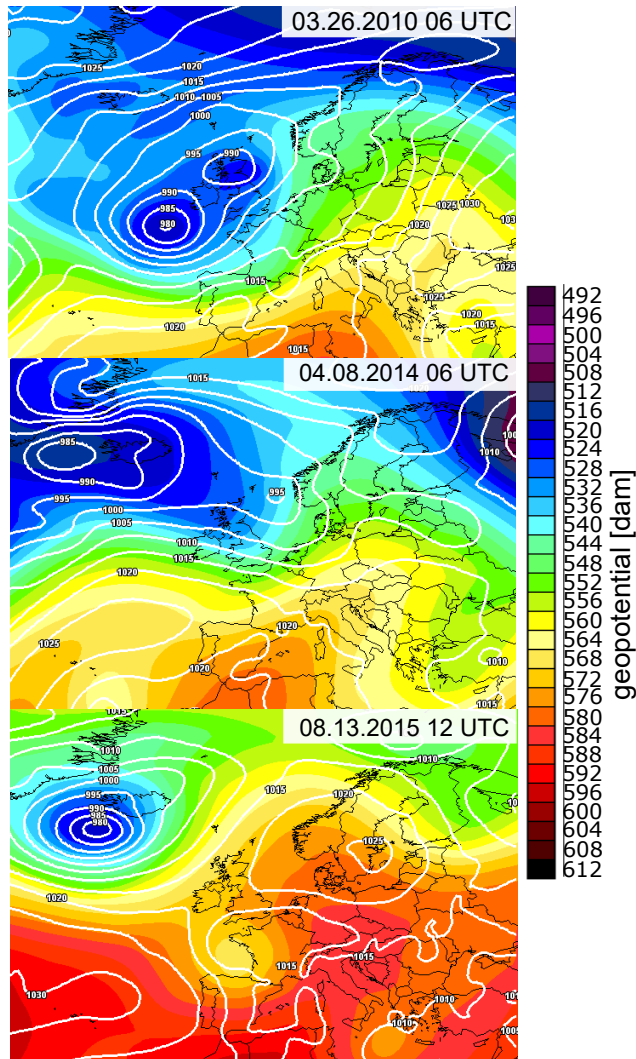[1]The Weissfluhgipfel radar was not yet installed at the time of the considered events

Figure 1. 500 hPa geopotentials and pressure at mean sea level for the three considered events

$1° \times 1° \times 500\text{m}$ radar bins. Reflectivity measurements are then converted to equivalent precipitation intensity with a $Z - R$ relationship. The precipitation estimation at the ground is extrapolated from multi-radar observations aloft using a weighting function that depends on the altitude above the ground and the radar visibility. Corrections for the vertical profile of reflectivity (VPR) is done with an average profile based on aggregation over a few hours and over the visible part of the area located less than 70 km around the radar. More information on the MeteoSwiss QPE estimation can be found in Germann et al. (2006). Note that the Plaine-Morte radar was only installed in 2014 and was thus not available during the first event (26 March 2010). The Swiss radar composite extends radially up to 250 km from every single radar (Figure 2). However, the quality of the product is better closer to the radar and
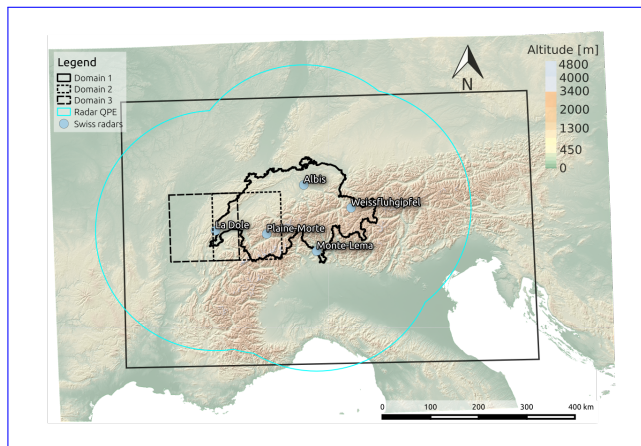
Figure 2. Situation map showing the theoretical maximum extent of available QPE (light blue), the Swiss operational radars (blue dots) as well as the region used for the climatological study of COSMO precipitation intensities (domain 1) and the sub-regions centered over the precipitation events used in the QPE analysis (domains 2 and 3)

in the areas where the radar scanning domains overlap. To perform a comparison of rain intensities a smaller field of 128x128 km^2 was chosen in the center of the domain where the quality of the product is optimal (Domain 2 in Figure 2). For the second event (8 April 2014) the domain was moved slightly to the left in order to better follow the evolution of the precipitation event (Domain 3 in Figure 2)

5 ## 3 The UM framework

3.1 Multifractality

Let ϵ be a normalized (divided by its mean) conservative field, which can be one or two dimensional (time series or spatial map). In the multifractal framework, ϵ_λ, the field at resolution λ is obtained by up-scaling the field measured or simulated at the maximum resolution to the resolution λ which is defined by the ratio between outer scale L and observation scale l ($\lambda = L/l$).

If ϵ is multifractal, its statistical moments q scale with resolution:

$$\langle \epsilon_\lambda^q \rangle \approx \lambda^{K(q)} \tag{3}$$

Where $K(q)$ is the moment scaling function. For a conservative field $\langle \epsilon_\lambda \rangle = 1$.

8

It can be shown (Schertzer and Lovejoy, 1987) that this is equivalent to the following relation between probabilities of falling below a certain threshold :

$$\Pr\left(\epsilon_\lambda \le \lambda^\gamma\right) \approx \lambda^{-c(\gamma)} \tag{4}$$

where $c(\gamma)$ is the co-dimension function which is convex and increasing, γ is a so-called singularity, which is independent of scale. λ^γ can thus be seen as a scale dependent threshold. The functions $K(q)$ and $c(\gamma)$ are related by a Legendre transform (Parisi and Frisch, 1985b).

The quality of this scaling can be studied with the Trace Moment (TM) method which consists for each moment q in a log-log plot of the up-scaled fields as a function of the resolution λ, the slope being the moment scaling function. The coefficient of determination corresponding to the best fit-line of the TM analysis performed with $q = 1.5$, which will be referred to as R^2 in this work, is often taken as an indicator of the quality of scaling ($R^2 \in [0,1]$).

In the universal multifractal framework (Schertzer and Lovejoy, 1987), the moment scaling function for a conservative field $K_c(q)$ can be fully characterized with only two parameters, α and C_1:

$$K_c(q) = \frac{C_1}{\alpha - 1}\left(q^\alpha - q\right) \tag{5}$$

C_1 is the mean intermittency co-dimension and measures the clustering of the (average) intensity at increasing scales. C_1 is equal to zero when the field is homogeneous. α is the multifractality index and measures the clustering variability with respect to the intensity level, $\alpha \in [0,2]$.

Figure A.1 in the appendix illustrates the effect of varying α and C_1 on randomly generated isotropic conservative multifractal fields. One can see how increasing α, increases the variability within non-zero intensity regions whereas increasing C_1 decreases the intermittency and makes the field look more spatially homogeneous.

The size of the sample limits the insight one can get of a statistical process. For multifractal processes, if N_s samples are available this will result in a maximum singularity γ_s and moment order q_s beyond which the values of the statistical estimates of the co-dimension and moment scaling function are not considered as reliable ((Schertzer and Lovejoy, 1987), (Lovejoy and Schertzer, 2007)). It can be shown that in the multifractal framework we have:

$$q_s = \left(\frac{D + D_s}{C_1}\right)^{\frac{1}{\alpha}} \quad \text{and} \quad \gamma_s = \alpha' C_1 \left(\frac{D + D_s}{C_1}\right)^{\frac{1}{\alpha'}} \tag{6}$$

where $\frac{1}{\alpha} + \frac{1}{\alpha'} = 1$, D is the dimension of the field (1 for a time series, 2 for a spatial field) and D_s is the sampling dimension defined by $N_s = \lambda^{D_s}$.

Example of the use of γ_s can be found in Royer et al. (2008) who investigated the impact of climate change on rainfall extremes using a climate model. They observed an increase of γ_s over time which could result in a possible increase in the intensity of rainfall extremes over the next hundred years. Douglas and Barros (2003) and Hubert et al. (1993) also used the maximum singularity γ_s in the estimation of probable maximum precipitation.

In order to perform a multifractal analysis the field ϵ needs to follow the following properties

1. The size N of the field needs to be the same in all dimensions i.e. $\epsilon \in \mathbb{R}^{N^D}$.

2. N needs to be a power of two.

In this work, the UM parameters are estimated with the Double Trace Moment (DTM) method (Lavallée et al., 1993). This method relies on the fact that in the context of UM, the moment scaling function $K(q,\eta)$ of the field $\epsilon_\lambda^{(\eta)}$, obtained by raising the field ϵ at a power η and up-scaled at resolution λ can easily be expressed as a function of α (Lavallée et al., 1993):

$$\left\langle \left(\epsilon_\lambda^{(\eta)} \right)^q \right\rangle \approx \lambda^{K(q,\eta)} = \lambda^{\eta^\alpha K(q)} \tag{7}$$

α is thus the slope of the linear part of $K(q,\eta)$ as a function of η in a log-log plot.

3.2 Non-conservative fields

In the case of a non-conservative field ϕ, we have $\langle \phi_\lambda \rangle \neq 1$.

One way to consider non-conservative fields within the UM framework it to assume that they can be expressed as:

$$\phi_\lambda = \epsilon_\lambda \lambda^{-H} \tag{8}$$

where H is the non-conservation parameter ($H = 0$ for conservative fields) and ϵ is a conservative field characterized by a moment scaling function $K_c(q)$ with parameters C_1 and α.

The moment scaling function of the non-conservative field ϕ_λ is then given by:

$$K(q) = K_c(q) - Hq \tag{9}$$

H can be related to the spectral slope β by:

$$\beta = 1 + 2H - K_c(2) \tag{10}$$

where β is the exponent of the power law that characterizes the relation between power spectrum and wave numbers:

$$E(k) \propto k^{-\beta} \tag{11}$$

Hence the larger the value of the slope β, the shorter the decorrelation range. If β is larger than the dimension of the field, the field is non-conservative.

ϵ_λ can be estimated from ϕ_λ with a fractional integration (for $H < 0$) or differentiation (for $H > 0$) of order H, which is equivalent to a multiplication by k^H in the Fourier space. In practice however, for $H > 0$, particularly when $H > 0.5$, $\epsilon_{\lambda_{\max}}$ (the field ϵ at the maximum resolution) is often approximated by the renormalized absolute fluctuations of the field.

$$\epsilon_{\lambda_{\max}}(i) = \frac{|\phi_{\lambda_{\max}}(i+1) - \phi_{\lambda_{\max}}(i)|}{\langle|\phi_{\lambda_{\max}}(i+1) - \phi_{\lambda_{\max}}(i)|\rangle}, \quad i = 1, 2, .., N \tag{12}$$

Figure A.2 in the appendix illustrates the effect of H on isotropic multifractal fields, with constant α and C_1. H can be considered as a kind of smoothness parameter, that denotes the order of integration ($H < 0$) or differentation ($H > 0$) needed to obtain the observed field from a direct multifractal cascade process.

Table 3 provides an overview of all multifractal parameters as well as their interpretation.

3.3   Spatio-temporal analysis

The multifractal analysis of time series of two-dimensional fields, such as the ones considered in this study, can be performed both in space, by considering an ensemble of two-dimensional fields (one sample for every time step) or in time, by considering an ensemble of one-dimensional time series (one sample for every coordinate in the two-dimensional field).

A simple spatio-temporal scaling model (e.g., Marsan et al., 1996; Deidda, 2000; Macor et al., 2007; Radkevich et al., 2008) is based on the hypothesis of an anisotropy coefficient between space and time:

$$K_{\text{space}}(q) = \frac{K_{\text{time}}(q)}{1 - H_t} \tag{13}$$

where H_t is the anisotropy coefficient between space and time, which in the theory of Kolmogorov (Kolmogorov (1962), Marsan et al. (1996)) is equal to 1/3. This result implies identical α and proportional C_1 and H parameters:

$$\frac{C_{1,\text{space}}}{C_{1,\text{time}}} = \frac{H_{\text{space}}}{H_{\text{time}}} = \frac{1}{1 - H_t} \tag{14}$$

4   Climatological analysis of multifractal parameters

4.1

Within all 209 selected squares (Section 2.2), the multifractal parameters α, C_1, β , H, γ_s, R^2 and D_f were computed both in space, using an ensemble average, i.e. by taking the mean parameters over all the available realizations of the process. In space we consider every timestep to a be a realization of a

Parameter	Name	Interpretation
α	multifractality index	When $\alpha = 0$, the field is mono-fractal which means that a single fractal dimension is sufficient to fully characterize the field. The higher α, the larger the variability within areas with precipitation.
C_1	mean intermittency	Measures how concentrated the average field is, $C_1 = 0$ for a uniform field. The larger C_1, the larger the intermittency of the field. High C_1 associated with high α implies strong extremes.
β	Negative of the spectral slope	The larger β the shorter the decorrelation range of the data. If $\beta = 0$, the power spectral density is the one of white noise, meaning there is no decorrelation. When β is large, large scale phenomena have a large contribution to the variability of the data, which means that the fields have a larger correlation range (smoother fields).
H	non-conservation parameter	Scale-independent proportionality factor relating a conservative field to the non-conservative field (a field for which the average is not scale independent). Can be seen as a smoothing factor. If H is positive, the field is too smooth and one needs to differentiate it to retrieve a conservative field. If H is negative, the field is too discontinuous and one needs to integrate it to retrieve a conservative field.
γ_s	maximum singularity	Maximum observable singularity (scale independent threshold) from the data. Large γ_s implies that stronger extremes are present in the data.
R^2	TM coefficient of determination	Coefficient of determination of the relation between a given moment of order q and the scale (Equation 3) on a loglog plot. If the field is multifractal, then the plot is a straight line with slope $K(q)$. In practice $q = 1.5$ is often used as a reference to determine R^2. R^2 can be seen as an estimation of the quality of scaling and of the viability of the multifractal approach for the data.
D_f	Fractal dimension	Factor relating the number of rainy observations at a given scale to the scale. The larger D_f, the more uniform the binary precipitation field (for a threshold of zero) is.

Table 3. Overview of all multifractal parameters

two-dimensional geophysical process and in time, we consider every COSMO gridpoint to be a realization of a one-dimensional geophysical process (time series). For the analysis in space this implies 43115 realizations of a 64x64 2D field and for the analysis in time 64x64 (= 4096) realizations of a timeserie of length 32768 (2^{15} which is the closest power of 2 of 43115). Analysis of the overall temporal power spectrum (not displayed) reveals the presence of a strong peak centered around a resolution of 3 hours, which is very likely to be caused by the nudging scheme of COSMO (assimilation within the model is performed every 3 hours). To remove the effect of the nudging in the estimation of multifractal parameters, only the larger time scales (from 8 hours to 5 years) were thus considered.

In

order to test the effect of zeros on the overall analysis, the multifractal parameters were also estimated in space by using only the fields where there is precipitation over at least 50% of the surface[2]. This did however not impact the main conclusions in terms of correlations and spatial structure of the multifractal parameters. Hence the subsequent study was performed on the

raw precipitation fields without any kind of filtering.

4.1   Correlation study

The relationship between MF parameters evaluated in time and space and the descriptors detailed in Table 1 was studied first by looking at the non-parameteric (Spearman) correlations. Figure 3 shows the correlation plots for the MF parameters in space and time.

4.2

The following conclusions can be drawn from the correlation plots. D_f is strongly correlated with the latitude indicating that the fractal dimension of rain is higher at higher latitudes (i.e. cooler climates). D_f is also quite strongly correlated to the wet fraction: the more often it rains, the higher the fractal dimension. Similarly C_1 also has a strong latitudinal trend and tends to decrease in regions with a high wet fraction (less intermittency) which is typically the case in cooler climates. α also seems to also have a latitudinal trend though not as strong as for C_1 and D_f. The link between α and the standard deviation is not obvious since the standard deviation is a second order statistic while the UM parameters are based on all moments. C_1 and γ_s tend to decrease with the altitude while β and H tend to increase. This could be due to orographic effects, precipitation over mountains being both dominated by large scale circulations and generally abundant. Synoptic descriptors such as the geopotential, the temperature and the potential vorticity do not seem to play a direct role on the multifractal parameters of precipitation and the observed correlations result merely from their correlations with the latitude and the altitude.

The correlation values are roughly consistent in time and in space, although the ones in time are generally higher. In time the correlation between β and H is much lower than in space. This can be explained by the lower values of β in time. Because of this and as a consequence of Equation 10, H becomes more correlated with α and C_1.

---

[2]In time, it would not be possible to filter out non rainy timesteps, as it would break the continuity of the time series.
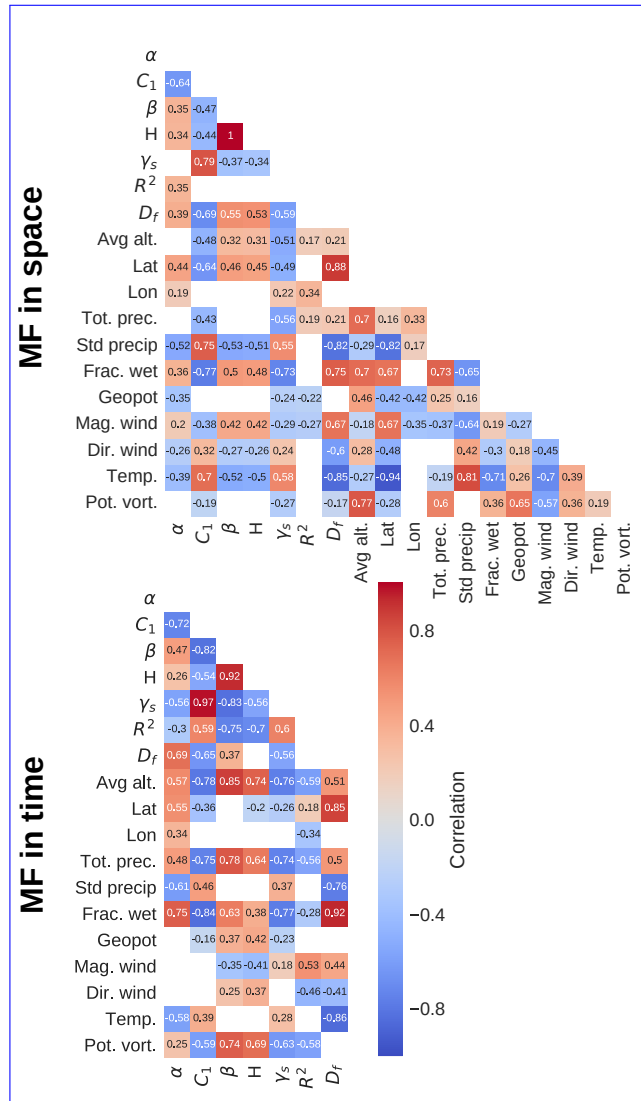
Figure 3. Correlation plots showing the Spearman (rank) correlation between MF parameters and descriptors. On the left with MF parameters estimated in space and on the right with MF parameters estimated in time. Note that the part on the right of the correlation plot in time has been truncated since it is the same as on the correlation plot in space. Correlations that are not statistically significant (for a significance level of 2.5%) are left in white.

In summary, the fractal dimension D_f is proportional to the fraction of wet simulations, which increases with the latitude and to a lesser extent with the altitude. The parameter β, which is proportional to the correlation range follows a similar trend, whereas the mean intermittency C_1 follows the inverse trend. In space α is difficult to characterize whereas in time it follows D_f and β to a certain extent.

4.2   Hierarchical clustering

A hierarchical clustering of all 209 areas was performed based on the value of their descriptors, using the Ward linkage method (Ward, 1963). Investigation of the dendrogram gives an optimal number of classes of either 3 or 6. Figure 4 shows the resulting classification for three different classes.
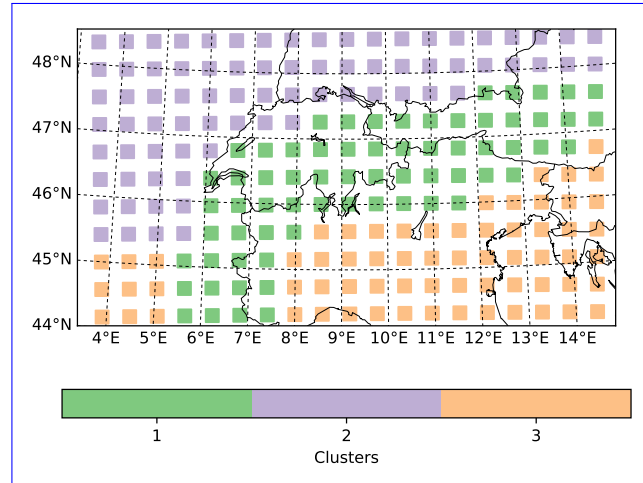

Figure 4. Result of the hierarchical clustering of the 209 regions into three classes

5   As could be expected, the clustering of the meteorological and geographic descriptors results into a meaningful spatial distribution. Indeed, all classes are spatially very coherent, with class 1 corresponding mostly to the Alpine regions, from the Mediterranean sea to Austria, class 2 corresponding mostly to the cooler temperate regions in the east of France and south of Germany (Cfb class in the famous Köppen (1936) climate classification) and class 3 corresponding to the warmer Mediteranean regions in the south of France, in Italy and the Balkans (Csa class in
10   the Köppen-Geiger classification).

The distributions of MF parameters within these clusters as illustrated in Figure 5 highlight some obvious discrepancies in MF parameters between clusters. In space, for example α, H, β and D_f seem to be much lower in cluster 3 than in the others while C_1 and γ_s are much higher. Clusters 1 and

4.3

15   2 do not show such spectacular differences but differ nonetheless by stronger values of D_f and slightly larger values of γ_s within cluster 2. In time, cluster 1 (Alpine regions) is characterized by high values of α and β and low values of C_1, which indicates frequent rainfall and a large variability in intensities. Clusters 2 and 3 differ by their low values of β and H indicating that, compared with alpine regions, the small temporal frequencies play a larger role in the overall variability.
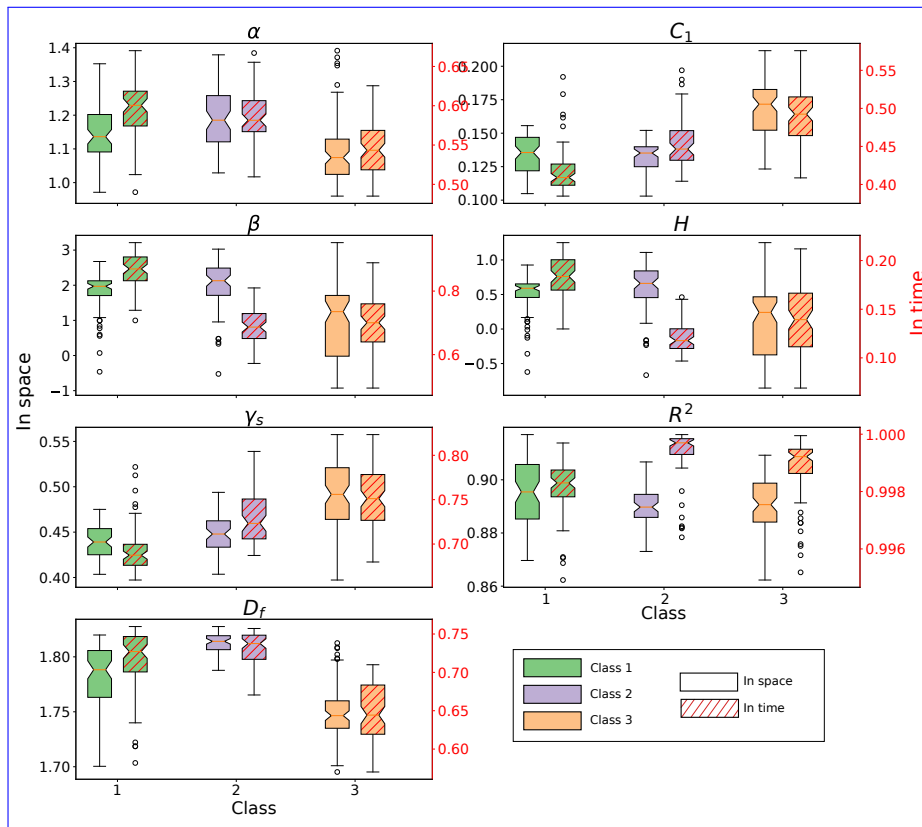
15

Figure 5. Boxplots showing the distributions of MF parameters within the clusters. MF parameters estimated in time are shown with a dashed pattern. Note that the left y-axis applies to MF parameters in space and the right y-axis (in red) to MF parameters in time (the boxplots indicated with a red hatch).

The statistical significance of these discrepancies was confirmed both with the MANOVA (multivariate anova) and the non-parameteric Kruskal-Wallis tests. All test were performed with a significance level of 2.5%. Note that the R^2 was not considered in this analysis as it is more a confidence indicator than a proper characteristic of an area. The MANOVA reveals that the multivariate means of MF parameters (both in time and space) are significantly different
5   between the three clusters as well as between all three pairs of clusters taken separately (1 vs 2, 2 vs 3 and 1 vs 3). The non-parameteric Kruskal-Wallis test performed separately for all MF parameters reveals that distributions of all MF parameters are significantly different between the three clusters. A pairwise comparison (1 vs 2, 2 vs 3 and 1 vs 3) reveals that in time all MF parameters are significantly different between all pairs of clusters, except for D_f which is not statistically different between clusters 1 and 2. In space the situation is similar but this time it is C_1
10   and γ_s which are not significantly different between clusters 1 and 2.

To summarize, the statistical analysis shows that the multifractal parameters of precipitation intensities are significantly different within the three climatological clusters.
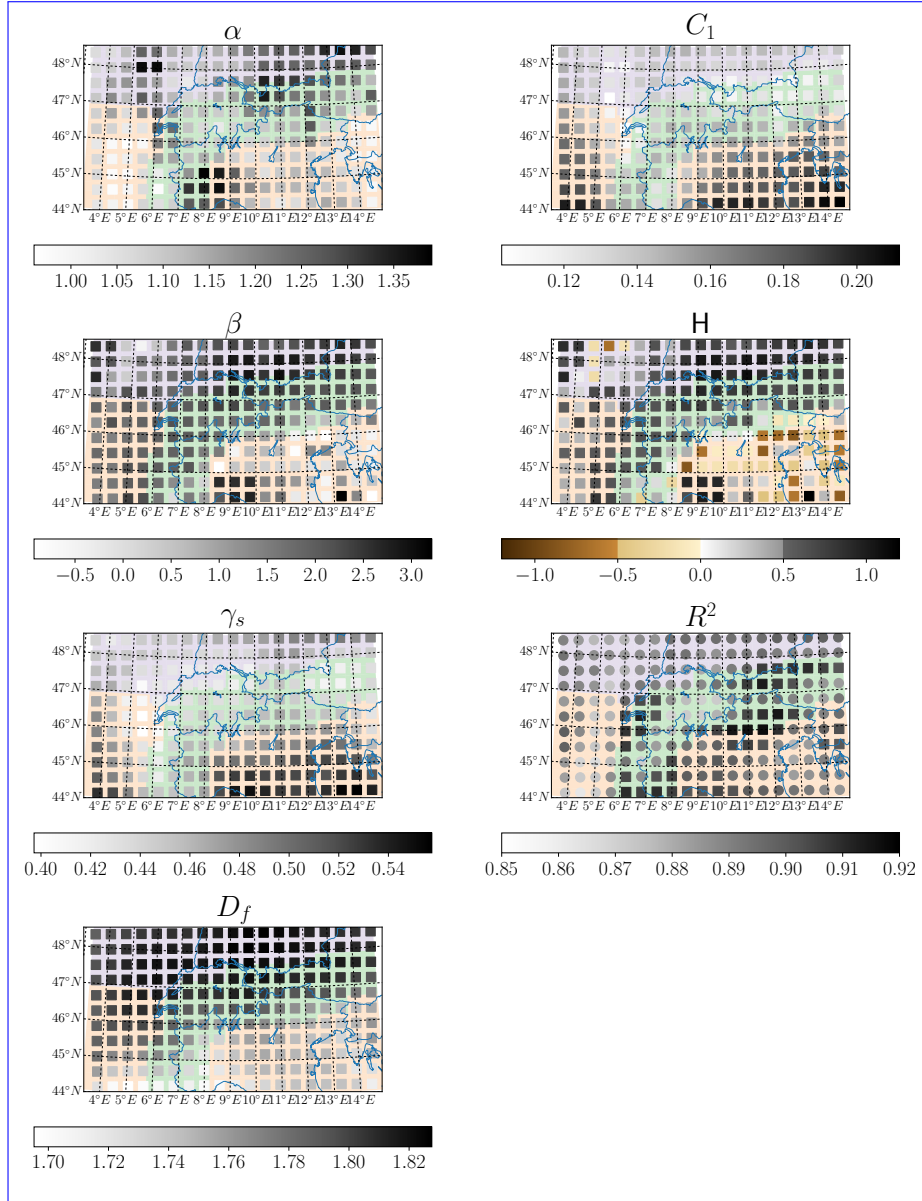
16

4.3 Spatial structure of MF parameters

Figure 6. Spatial representation of the MF parameters estimated in space for all areas. The special colormap for H has been chosen to separate positive and negative values and highlight non-conservative areas where $|H| > 0.5$. Note that as before, the size of the represented squares is not to scale. The colors in the background correspond to the hierarchical classification.

The analysis of the spatial structure of MF parameters in space reveals that α is particularly large over Bavaria, the Piemont region of Italy and the Champagne region of France. However these "clusters" of large values are somewhat difficult to relate to other trends, especially in terms of descriptors. Generally the Swiss Alps are characterized by relatively low values of α. In terms of C_1 there is a clearer trend, with a strong latitudinal and altitudinal negative gradient, which can be related to an increase in

overall precipitation amounts. In terms of β, the regions over Italy show smaller values, which tend to indicate that precipitation events exhibit strong high-frequency components (such as for example short convective storms). Over the Alps and the more continental regions, where the precipitation systems are mostly frontal, β increases. The trend is similar for H which is related to β. For γ_s, we observe a similar trend to C_1 with a decrease with altitude and elevation. This indicates that precipitation extremes are stronger in southern regions. For R^2 it is difficult to identify a proper spatial organization, except that the foothill regions of the Alps generally have large R^2 values. Finally for D_f, there is mostly a latitudinal trend. The value of D_f increase with the latitude, which can be related with the decrease in the number of zeros (smaller C_1 and generally larger α).

In time (not displayed), similar conclusions can be drawn for C_1, D_f, γ_s and β. For the other parameters the latitudinal trend seems to be much more visible than in space, especially for H and R^2. R^2 seems to be generally larger in time than in space with values close to 1. Unlike in space, for α in time there is a clearer dependency on the altitude. α in time tends to be larger in mountainous regions, indicating a larger temporal variability of precipitation intensities in these regions.

To summarize, the multifractal signature of precipitation is related both to the topography, the climate and the typical synoptic conditions and as such can be used as a way to characterize precipitation fields and to assess the realism of simulated atmospheric variables.

5 Comparison of simulated precipitation with radar QPE

The previous section presented the MF approach in a rather climatological perspective, that helps to link meteorology/geography and MF parameters. In the present section, we evaluate the quality of the precipitation simulated by COSMO with two different microphysical schemes by means of the UM tool and by comparison with quantitative precipitation estimations from the Swiss radar network. Instead of simply retrieving simulations from the MeteoSwiss archives this comparison requires to actually run the COSMO model at the radar temporal resolution in a very expensive set-up (two-moments scheme). As such a climatological comparison as in the first part is not feasible from a computational point of view. Because of this and in order to better capture the microphysical aspects, the comparison is now conducted at the event scale.

5.1 Scaling analysis

A multifractal comparison of the precipitation fields simulated by COSMO in its one-moment and two-moments schemes with the QPE product from the Swiss radar composite was performed. As a first step, a spectral analysis was performed both in time (ensemble of one-dimensional time series of precipitation intensities) and space (ensemble of two-dimensional maps of precipitation intensities).
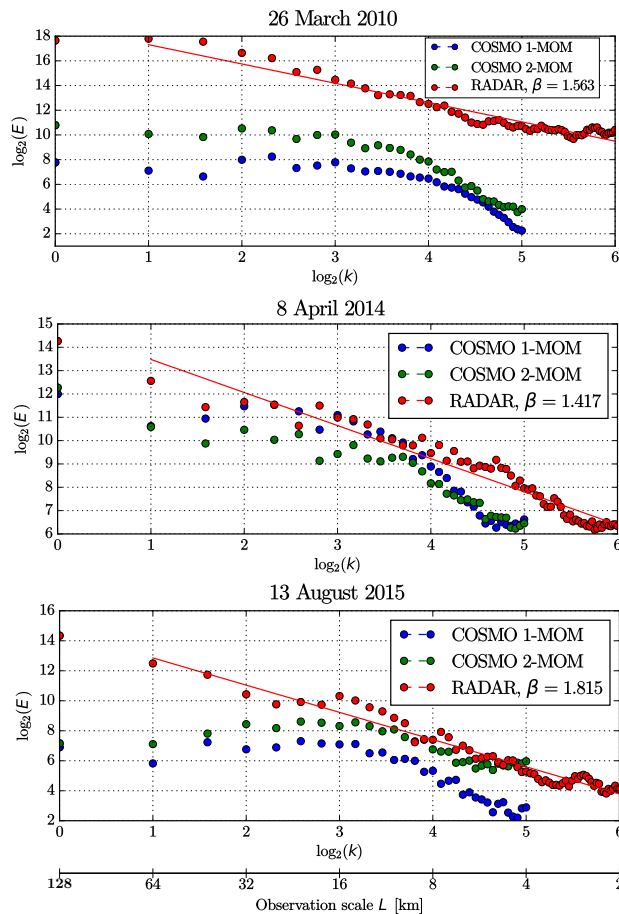

Figure 7. Spectral analysis in space of the QPE products during the three events. Bold lines are best-fit lines. The associated value of β is given in the legend. Note that the maximal represented observation scale, which corresponds to the Nyquist frequency, is twice the maximal resolution.

Figure 7 shows the spectral analysis in space for all events and data. A best-fit line is shown for the radar QPE from which the value of β is computed. β is equal to $-m$, where m is the slope of the best-fit line.

For the 26 March 2010, we observe a single scaling regime for the radar QPE, with a good scaling both at large (16-64 km) and small scales (2-16 km), as the spread around the line is relatively small. For the model intensities, we observe strong discrepancies in spectral slope with the radar QPE at smaller scales ($4-8$ km) which are not well represented. A possible explanation for this break in scaling properties of the model, is the fact that large scales are dominated by the dynamics of the model (primitive equations of the atmosphere) whereas smaller scales are dominated by the parameterizations of sub-grid phenomena (turbulence, convection). However, even at larger scales (8-64 km), the agreement between radar QPE and model simulations is still quite poor in terms of spectral slope. Obviously, for this rainfall event, COSMO is not able to recreate the spatial structure of precipitation observed by the radar.

For the 8 April 2014, the scaling is similar between radar and model precipitation intensities, possibly indicating that for this stratiform rain event, parameterizations and dynamics match better. Both radar and simulations show a weak scaling break at around 8 km.

For the last event, we observe again a good scaling for the radar QPE and a much worse scaling on the model precipitation intensities, but in contrast with the first event, this time the larger scales (> 16 km) are not well represented. Indeed, inspection of the time series of precipitation shows that COSMO is not able to locate accurately the convective cells of precipitation and generally overestimates their extent. In terms of microphysical parameterizations, we observe that the spectral slopes of the one-moment scheme are generally closer to the ones obtained from the radar QPE. This is especially visible for the last (convective) event, where the COSMO simulations show weak scaling (β close to zero). This implies that the simulated rainfall intensities are dominated by small-scale features, while large scale features are underestimated. Note also that for large scale features, the power density function of COSMO simulations correspond to white noise, indicating that the COSMO model has a shorter decorrelation range than the radar data.

The spectral analysis in time (not displayed) generally shows similar results, but with larger values of β and overall better scaling (less spread).

Table 4 displays the non-conservation parameters H evaluated for time series of precipitation intensities (analysis in time) and for spatial fields of precipitation intensities (analysis in space), for both the radar QPE (in regular font), the COSMO one-moment scheme (in bold) and the COSMO two-moments scheme (in italic). A value of H larger than 0 indicates that the field is smoother than the observed field from a direct multifractal cascade process and a value of H smaller than 0 indicates that the field is too discontinuous. Taking the radar as reference, one sees that the convective event is characterized by the largest values of H followed by the snowfall event and the stratiform event. When comparing H between COSMO and the radar QPE, one observes that H in time is always larger with the one-moment than on the radar QPE, indicating that the temporal structure of the simulated fields is likely to be too smooth. In space the trend is not as obvious and the match between radar QPE and one-moment scheme seems better.

Overall, it is worth noticing that the two-moment scheme almost always has smaller H values than the one-moment scheme, which indicates that it is more discontinuous both in time and space.

In order to account for the fact that the fields are mostly non-conservative $(|H| > 0.5)$ and to treat all fields in a consistant way, all further analysis was performed on fluctuations of the original fields (Equation 12). Note that while this does not result in perfectly conservative fields, it still makes them more conservative since all values of $|H|$ are smaller than 0.5 after taking the fluctuations.

	26 March 2010	8 April 2014	13 August 2015
H_{space}	0.411/**0.432**/*0.752*	0.342/**0.500**/*0.260*	0.651/**0.612**/*0.332*
H_{time}	-0.044/**0.615**/*0.262*	0.232/**0.938**/*0.238*	0.696/**0.818**/*0.265*

Table 4. Values of the non-conservation parameter H in time and space for all events, for the radar QPE, the COSMO **one-moment scheme** and the COSMO *two-moment scheme*.
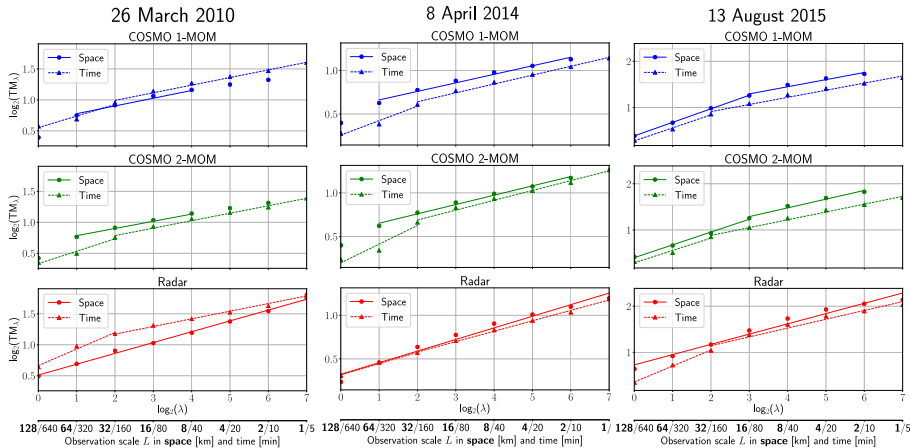

Figure 8. Scaling analysis of the QPE product during the three events. Bold lines are best-fit lines taking into account a possible scaling break.

Figure 8 shows the trace-moment (TM) analysis in time and space of the three events. For the two first events a scaling break can be observed at large scales for the COSMO intensities (64-128 km). These scales were excluded from the analysis, due to the limited number of points in this scale range. For the first event, in order to be consistent with the observations of the spectral analysis, the scale range 2-8 km, which does not scale well on COSMO simulations when compared with radar observation, was excluded from the analysis. For the last event, two scaling regimes are observed for the COSMO intensities, (2-16 and 16-128 km), which were studied separately. On the opposite, for the radar QPE no scaling break is observed in space. In time, a weak scaling break can be observed both for radar and COSMO intensities at a resolution of around 160 minutes, which corresponds roughly to the assimilation frequency

21

of the model (every three hours). Hence results are discussed only for the time scales between 5-160 min (smaller scales). Note that in the considered range of scales the quality of scaling measured by the R^2 parameter is quite good (average R^2 in space $= 0.963 \pm 0.024$, in time 0.956 ± 0.017. This implies that the uncertainty associated with the α and C_1 parameters retrieved with the DTM method is small.

5.2 Spatio-temporal analysis

Values of α, C_1 and γ_s obtained with an analysis in time and in space of the three events are given in Figure 9. For the first two events, all parameters are computed only on the smaller scales (up to 64 km in space and up to 160 minutes in time), in order to account for the observed scaling break. For the last event both scale ranges are considered.
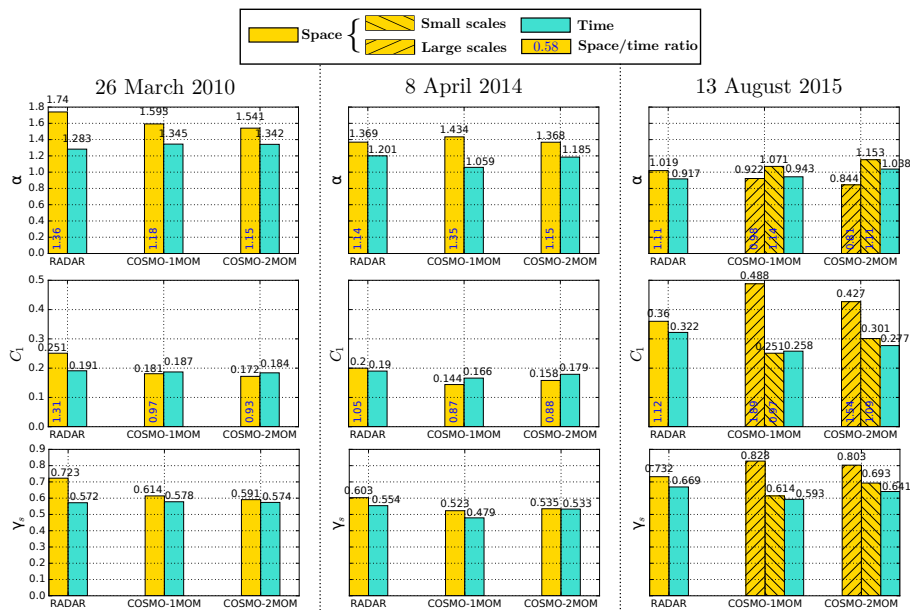
Figure 9. α, C_1 and γ_s parameter values obtained with an analysis in time and space for the three events on the fluctuations of the precipitation intensities. For the last event both the parameters at large and small spatial scales are displayed. The numbers in blue are the space/time ratios for α and C_1

For the first event, both COSMO microphysical schemes give very similar multifractal parameters and the discrepancy with the radar QPE is quite important. In space, it can be observed that α is slightly smaller in the COSMO simulations than on the radar QPE. It is clear as well that the simulated C_1 is too small compared with the radar observations. This tends to indicate that COSMO is underestimating the spatial intermittency. Generally, the observed discrepancies in α and C_1 tend to indicate that the spatial structure of the simulated fields is too smooth and lacks the variability observed by the radars. In time, the agreement is better for C_1 but COSMO

22

has clearly higher values of α indicating a larger temporal variability than the radar QPE. For this event, there is a noticeable discrepancy between the maximum singularity γ_s in space obtained from the radar QPE (0.721) and the γ_s obtained from the model (around 0.6 for both schemes). This indicates that during this event COSMO had a tendency to under-estimate extreme values, which might be caused by its difficulty to accurately simulate snowfall events, since COSMO does not consider partially melted snow (Frick and Wernli, 2012). Note that QPE in snow is very difficult and it is likely that the radar QPE itself is already underestimating precipitation intensities (Speirs et al., 2016) which would make this difference in γ_s even more noteworthy.

For the stratiform rain event, the multifractal parameters of the COSMO simulations are in better agreement with the radar QPE. In time, the two-moment COSMO scheme gives values that are in relatively close agreement with the radar QPE and in this regard outperforms the one-moment scheme. COSMO simulations show generally smaller values of α and smaller values of C_1 than the radar QPE which is a trend that is observed for all events.

For the last convective event, two scaling regimes are considered in space, larger scales (16-128 km) and smaller scales (2-16 km). As already observed in the spectral analysis there is a better agreement between the radar observations and the simulations with the one-moment scheme at smaller spatial scales. In time however, the temporal intermittency of COSMO is smaller than for the radar QPE, which can be explained by the fact that COSMO generally overestimates the extent of the convective systems. Compared with the one-moment scheme and the radar QPE, the two-moment scheme has a smaller α in space but a larger α in time, as well as a a smaller intermittency in time and space.

In summary, the observations of the spatio-temporal analysis are consistent with the spectral and scaling analysis where (1) a strong discrepancy in scaling behaviour was observed between COSMO and the radar QPE at small scales for the first event,(2) a better scaling of the model precipitation intensities was observed for the second event, (3) a discrepancy in scaling at large scales was observed between COSMO (especially for the two-moment scheme) and the radar QPE for the third event.

Overall, it can be observed that except for the first event where both schemes give similar values, the two-moment scheme is usually characterized by a larger C_1 than the one-moment scheme, both in time and space, whereas in terms of α there is no recurring trend. For the multifractal parameters α and C_1, there is generally a good agreement between radar observations and simulations on the range of scales where the model exhibits a good scaling behaviour, with none of the two microphysical schemes performing significantly better than the other. The two-moment scheme however is generally characterized by a slightly larger maximum singularity γ_s indicating a better capacity to simulate extreme values. This is especially visible in the last convective event. In terms of space/time ratios, the observed ratios differ significantly from the theoretical model: the α space/time ratio is always larger and the C_1 space/time ratio always smaller than the theoretical values (1 and 1.44 respectively).

5.3

Gires et al. (2011) found different breaks for a Cevenol event (strong precipitation events occuring in Fall in the South of France), i.e. roughly 16 km in space and 1h in time, and a better agreement with a simple space time model but only for large scales which are not the primary focus of this study. These differences could be associated with the fact that the topography of the area analysed in this paper is more pronounced than in Gires et al. (2011). It should also be noted that the values of UM parameters α and C_1

on the relevant range of scales exhibit a better agreement between observations and model simulations in this paper.

5.3 Timeseries of multifractal parameters

To study the time series of multifractal parameters, we will focus on the third (convective) event, which shows the largest temporal variability. Comparison with the other events showed that the conclusions drawn for the third event in terms of discrepancies between radar and model multifractal parameters can be generalized to the second (stratiform) event and to a lesser extent to the first event (snowstorm).

Figure 10 shows the timeseries of α and C_1 throughout the third (convective) event for the COSMO and the radar QPE precipitation intensities, as well as some illustrative precipitation fields that will be discussed.

13 August 2015

For the convective event, four different phases can be identified. In the first short phase (12:00-14:00), observations and simulations agree relatively well in α and C_1. This period corresponds to the initial stages of the event when only a few isolated cells are present (panel (*a*) in Figure 10).

In the second phase (14:00 - 17:00), a large convective system is crossing the domain on the radar observations, which causes a strong increase in α and a decrease in C_1. This convective system is however located more in the south on the simulation and enters the domain only at around 15:30 (panel (*b*) in Figure 10).

During the third phase (17:00-21:00), the large convective system is visible on the simulated field, whereas on the observed radar fields, the most intense convective cells are already out of the domain. This causes a larger α on the simulations than on the observations (panel (*c*) in Figure 10). Finally in the last phase (21:00-24:00), a new convective system is visible on the observed field but is more or less absent on the simulated fields. This causes a discrepancy, the simulated fields having a smaller α and a larger C_1 than the observations (panel (*d*) in Figure 10). For this event, the spatial and temporal shifts of the convective system simulated by COSMO with respect to the radar observations is the main cause in the bad scaling observed at larger scales.

This succession of phases is also clearly visible in the timeseries of wet area fraction (Figure 11)

For the second event (stratiform rain), the conclusions are similar, discrepancies in multifractal parameters between simulated and observed precipitation intensities, are caused primarily by temporal and spatial shifts in the simulated precipitation patterns. The effect of such shifts on the multifractal analysis hints at the possibility of a further analysis based not on a fixed study domain but on a study domain following the precipitation system, in a way similar to
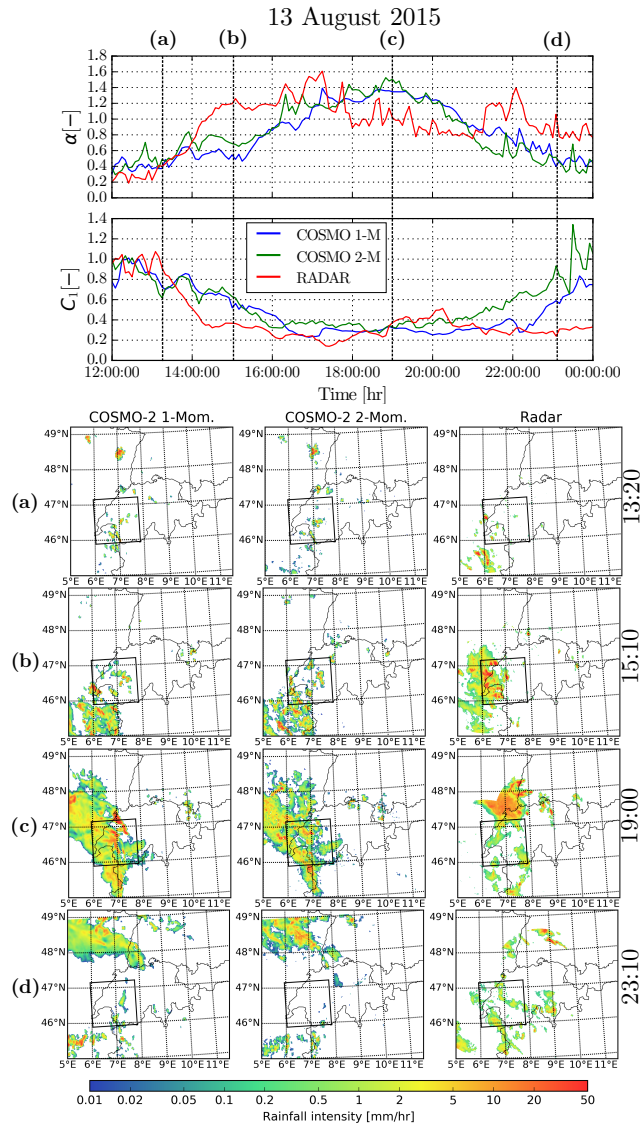
Figure 10. α and C_1 timeseries during event 3.

Nykanen and Harris (2003). This would allow to gain a better insight into the representation of small-scale structures by the model.

For the first event (snowstorm), an additional bias comes from the fact that the model tends to miss small-scale structures of precipitation particularly over mountainous regions (c.f. Figure 12), which can explain the observed strong difference in scaling between radar and model at smaller scales.
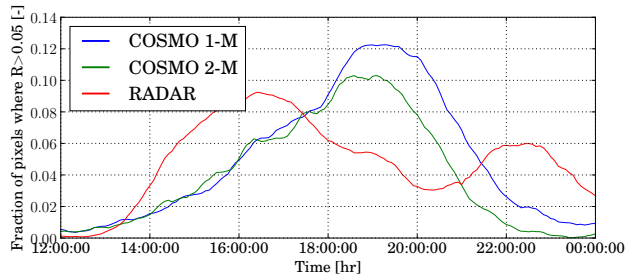
25

Figure 11. Fraction of wet area during the event of the 13 August 2015
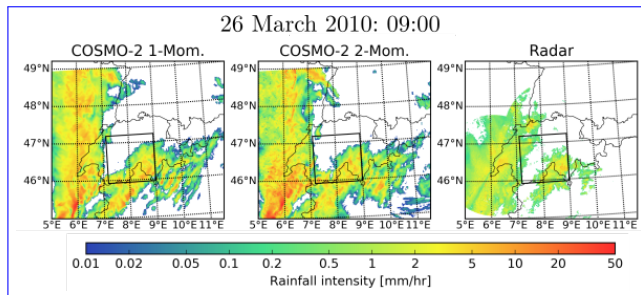
Figure 12. One snapshot of precipitation during the first event (snowstorm) illustrating how COSMO tends to miss small-scale precipitation cells (in the center of the domain). This behaviour is generalized during the whole event.

6 Conclusions

In this work we performed a spatial and temporal analysis of precipitation intensities simulated by the COSMO NWP model, in the context of the universal multifractal (UM) framework which allows to represent the variability across scales with a limited number of parameters.

The first part of this work focused on a climatological study of precipitation intensities simulated by COSMO in its operational analysis mode using multifractals. Analysis of the correlations between multifractal parameters and external meteorological and topographic descriptors reveals that the fractal dimension (D_f) and the mean intermittency (C_1) are strongly correlated to the fraction of rainy simulations. Additionally the fractal dimension tends to increase and the mean intermittency to decrease with the latitude, which indicates that rainfall fields are more homogeneous at higher latitudes. The effect of topography is visible in the values of C_1 and the maximum singularity γ_s (related to extreme values) which tend to decrease with altitude as well as with in the values of H and β which tend to increase with altitude. This indicates a smaller intermittency and less rainfall extremes in mountainous regions as well as smoother rainfall intensity fields, which can be linked to the dominance of large-scale orographic effects. A hierarchical clustering was performed based on the meteorological and topographic descriptors. The resulting classification into three classes was shown to correspond well with the famous Köppen (1936) climate

26

5 classification. Distributions of multifractal parameters within these three classes were found to be statistically significantly different, indicating that the multifractal signature of rain is indeed climate dependent. Finally, investigation of the spatial structure of multifractal fields confirmed the observations of the correlation analysis, namely that the values β and H are mostly influenced by the altitude (simulated precipitation tends to be smoother at higher altitudes) and D_f and C_1 are mostly influenced by the latitude (the intermittency decreases with the latitude).

10 The second part of this work focused on three different events, one cold front associated with heavy snowfall, one stationary front associated with stratiform rain and a stable atmosphere and one summer convection event with heavy rain. All events were simulated at a 2 km resolution with both the standard operational one-moment microphysical parameterization of COSMO and a more advanced two-moment microphysical scheme. A comparison between the multifractal signature of precipitation intensities at the ground simulated by COSMO with the Swiss

15 radar composite data was performed. Whereas the radar data shows one single scaling regime over the studied spatial scale ranges (1-128 km), the COSMO simulations display scaling breaks for the first and the last event. It can be observed that during the snowstorm event COSMO is unable to properly reproduce radar observations at small scales, which might be caused by the intrinsic difficulty of simulating solid precipitation. During the last convective event, the opposite can be observed, and COSMO is struggling to reproduce the larger scales, due to its difficulty to

20 locate properly the convective system in time and space during this event. In the temporal scales, a scaling break is observed both for the radar and COSMO simulations at around 3 hours, which corresponds to the assimilation frequency of the model. Comparisons of the one-moment and two-moment COSMO microphysical parametrizations show that the fields simulated by the two-moments scheme tend to display a larger intermittency and variability than the one-moment scheme. However, this does generally not translate into a better agreement of multifractal

25 parameters with the radar composite, except during the stratiform event where the two-moment scheme performs slightly better.

Ultimately, the multifractal framework can be used to identify the scale ranges in which the model is able to simulate realistic fields of water contents and as such this technique can be used as a diagnostic tool for model evaluation.

References

Baldauf, M., Seifert, A., Förstner, J., Majewski, D., Raschendorfer, M., and Reinhardt, T.: Operational convective-scale numerical weather prediction with the COSMO model: description and sensitivities, Mon. Weather Rev., 139, 3887–3905, doi:10.1175/MWR-D-10-05013.1, 2011.

5 Bohme, T., Van Lipzig, N., Delobbe, L., and Seifert, A.: Precipitation patterns above Belgium using weather radar and COSMO model reflectivity data, in: Proceedings of the 8th International Symposium on Tropospheric Profiling, Delft, The Netherlands, http://www.ch2011.ch/pdf/CH2011reportHIGH.pdf, 2009.

COSMO: COSMO namelists and variables, http://www.cosmo-model.org/content/tasks/operational/nmlDoc/cosmoDefault.htm?ver=3&mode=printerFriendly,

10 2015.

Davis, C., Brown, B., and Bullock, R.: Object-based verification of precipitation forecasts. part i: methodology and application to mesoscale rain areas, Mon. Weather Rev., 134, 1772–1784, doi:10.1175/MWR3145.1, 2006.

Deidda, R.: Rainfall downscaling in a space-time multifractal framework, Water Resour. Res., 36, 1779–1794, doi:10.1029/2000WR900038, 2000.

15 Doms, G., Förstner, J., Heise, E., Herzog, H., Mironov, D., Raschendorfer, M., Reinhardt, T., Ritter, B., Schrodin, R., Schulz, J.-P., et al.: A description of the nonhydrostatic regional COSMO model, Part II: Physical Parameterization, http://www.cosmo-model.org/content/model/documentation/core/cosmoPhysParamtr.pdf, accessed 04.08.2015, 2011.

Douglas, E. M. and Barros, A. P.: Probable maximum precipitation estimation using multifractals: application in the eastern United States, J. Hydrometeorol., 4, 1012–1024, 2003.

20 Ebert, E. E.: Fuzzy verification of high-resolution gridded forecasts: a review and proposed framework, Met. Apps, 15, 51–64, 2008.

Frick, C. and Wernli, H.: A Case Study of High-Impact Wet Snowfall in Northwest Germany (25-27 November 2005): Observations, Dynamics, and Forecast Performance, Weather Forecast., 27, 1217–1234, doi:10.1175/WAF-D-11-00084.1, 2012.

25 Gal-Chen, T. and Somerville, R. C. J.: On the use of a coordinate transformation for the solution of the Navier-Stokes equations, J. Comput. Phys., 17, 209–228, 1975.

Germann, U., Galli, G., Boscacci, M., and Bolliger, M.: Radar precipitation measurement in a mountainous region, Q. J. R. Meteorol. Soc., 132, 1669–1692, doi:10.1256/qj.05.190, 2006.

Gilleland, E., Ahijevych, D., Brown, B. G., Casati, B., and Ebert, E. E.: Intercomparison of spatial forecast verification

30 methods, Weather Forecast., 24, 1416–1430, doi:10.1175/2009WAF2222269.1, 2009.

Gires, A., Tchiguirinskaia, I., Schertzer, D., and Lovejoy, S.: Multifractal and spatio-temporal analysis of the rainfall output of the Meso-NH model and radar data, Hydrol. Sci. J., 55, 2011.

Gires, A., Tchiguirinskaia, I., and Schertzer, D.: Multifractal comparison of the outputs of two optical disdrometers, Hydrological Sciences Journal, 2015a.

35 Gires, A., Tchiguirinskaia, I., Schertzer, D., and Berne, A.: 2DVD Data Revisited: Multifractal Insights into Cuts of the Spatiotemporal Rainfall Process, J. Hydrometeorol., 16, 548–562, 2015b.

Hubert, P., Tessier, Y., Lovejoy, S., Schertzer, D., Schmitt, F., Ladoy, P., Carbonnel, J., Violette, S., and Desurosne, I.: Multifractals and extreme rainfall events, Geophys. Res. Lett., 20, 931–934, 1993.

Kolmogorov, A. N.: A refinement of previous hypotheses concerning the local structure of turbulence in viscous incompressible fluid at high Reynolds number, J. Fluid. Mech., 13, 82–85, 1962.

5 Köppen, W.: Das geographische System der Klimate, Allgemeine Klimalehre, Borntraeger, https://books.google.ch/books?id=hM2uugAACAAJ, 1936.

Lavallée, D., Lovejoy, S., and Ladoy, P.: Nonlinear variability and landscape topography: analysis and simulation, in: Fractals in geography, edited by de Cola, L. and Lam, N., pp. 171–205, Prentice-Hall, 1993.

Lin, Y.-L., Farley, R. D., and Orville, H. D.: Bulk Parameterization of the Snow Field in a Cloud Model, Journal of Climate

10 and Applied Meteorology, 22, 1065–1092, doi:10.1175/1520-0450(1983)022<1065:BPOTSF>2.0.CO;2, 1983.

Lovejoy, S.: COSMO namelists and variables, http://www.physics.mcgill.ca/~gang/multifrac/multifractals/isotropic.htm, 2017.

Lovejoy, S. and Schertzer, D.: Scaling and multifractal fields in the solid earth and topography, Nonlinear Proc. Geoph., 14, 465–502, doi:10.5194/npg-14-465-2007, 2007.

15 Macor, J., Schertzer, D., and Lovejoy, S.: Multifractal methods applied to rain forecast using radar data, La Houille Blanche - Revue internationale de l'eau, pp. 92–98, doi:10.1051/lhb:2007052, 2007.

Marsan, D., Schertzer, D., and Lovejoy, S.: Causal space-time multifractal processes: Predictability and forecasting of rain fields, Journal of Geophysical Research: Atmospheres, 101, 26 333–26 346, doi:10.1029/96JD01840, 1996.

Mellor, G. L. and Yamada, T.: Developement of a turbulence closure model for geophysical fluid problems., Rev. Geophys.

20 Space Phys., 20, 851–875, 1982.

Mittermaier, M., Roberts, N., and Thompson, S. A.: A long-term assessment of precipitation forecast skill using the Fractions Skill Score, Met. Apps, 20, 176–186, doi:10.1002/met.296, 2013.

Nykanen, D. K. and Harris, D.: Orographic influences on the multiscale statistical properties of precipitation, Journal of Geophysical Research: Atmospheres, 108, doi:10.1029/2001JD001518, 8381, 2003.

25 Parisi, G. and Frisch, U.: "On the singularity structure of fully developed turbulence, Turbulence and Predictability in Geophysical Fluid Dynamics and Climate Dynamics, pp. 84–88, 1985a.

Parisi, G. and Frisch, U.: A multifractal model of intermittency, North-Holland, 1st edn., 1985b.

Radkevich, A., Lovejoy, S., Strawbridge, K. B., Schertzer, D., and Lilley, M.: Scaling turbulent atmospheric stratification. III: Space–time stratification of passive scalars from lidar data, QJRMS, 134, 317–335, doi:10.1002/qj.203, 2008.

30 Rogers, R. R., Baumgardner, D., Ethier, S. A., Carter, D. A., and Ecklund, W. L.: Comparison of Raindrop Size Distributions Measured by Radar Wind Profiler and by Airplane, JAM, 32, 694–699, doi:10.1175/1520-0450(1993)032<0694:CORSDM>2.0.CO;2, 1993.

Royer, J.-F., Biaou, A., Chauvin, F., Schertzer, D., and Lovejoy, D.: Multifractal analysis of the evolution of simulated precipitation over France in a climate scenario, Comptes Rendus Geoscience, 340, 431 – 440,

35 doi:http://dx.doi.org/10.1016/j.crte.2008.05.002, 2008.

Rudledge, S. A. and Hobbs, P.: The Mesoscale and Microscale Structure and Organization of Clouds and Precipitation in Midlatitude Cyclones. VIII: A Model for the "Seeder-Feeder" Process in Warm-Frontal Rainbands, J. Atmos. Sci., 40, 1185–1206, doi:10.1175/1520-0469(1983)040<1185:TMAMSA>2.0.CO;2, 1983.

Schertzer, D. and Lovejoy, S.: Physical modeling and analysis of rain and clouds by anisotropic scaling multiplicative processes, J. Geophys. Res., 92, 9693–9714, 1987.

Schertzer, D. and Lovejoy, S.: Multifractals, generalized scale invariance and complexity in geophysics, 21, 3417–3456, 2011.

Schmitt, F., Lovejoy, S., and Schertzer, D.: Multifractal analysis of the Greenland ice-core project climate data, Geophys.

5   Res. Lett., 22, 1689–1692, doi:10.1029/95GL015221, 1995.

Seifert, A. and Beheng, K. D.: A two-moment cloud microphysics parameterization for mixed-phase clouds. Part 1: Model description, Meteorol. Atmos. Phys., 92, 45–56, doi:10.1007/s00703-005-0112-4, 2006.

Speirs, P., Gabella, M., and Berne, A.: A comparison between the GPM dual-frequency precipitation radar and ground-based radar precipitation rate estimates in the Swiss Alps and Plateau, Journal of Hydrometeorology, 18,

10   1247–1269, doi:10.1175/JHM-D-16-0085.1, 2016.

Vasić, Z., Lin, C. A., Zawadzki, I., Bousquet, O., and Chaumont, D.: Evaluation of precipitation from numerical weather prediction models and satellites using values retrieved from radars, Mon. Weather Rev., 135, 3750–3766, doi:10.1175/2007MWR1955.1, 2007.

Ward, J. H. J.: Hierarchical Grouping to Optimize an Objective Function, J. Am. Stat. Assoc., 58, 236–244,

15   doi:10.1080/01621459.1963.10500845, 1963.

Wernli, H., Paulat, M., Hagen, M., and Frei, C.: SAL - A novel quality measure for the verification of quantitative precipitation forecasts, Mon. Weather Rev., 136, 4470–4487, doi:10.1175/2008MWR2415.1, 2008.

Wicker, L. J. and Skamarock, W. C.: Time-splitting methods for elastic models using forward time schemes, Mon. Weather Rev., 130, 2088–2097, 2002.

Appendix A: Visual example of the effect of multifractals on the structure of a field
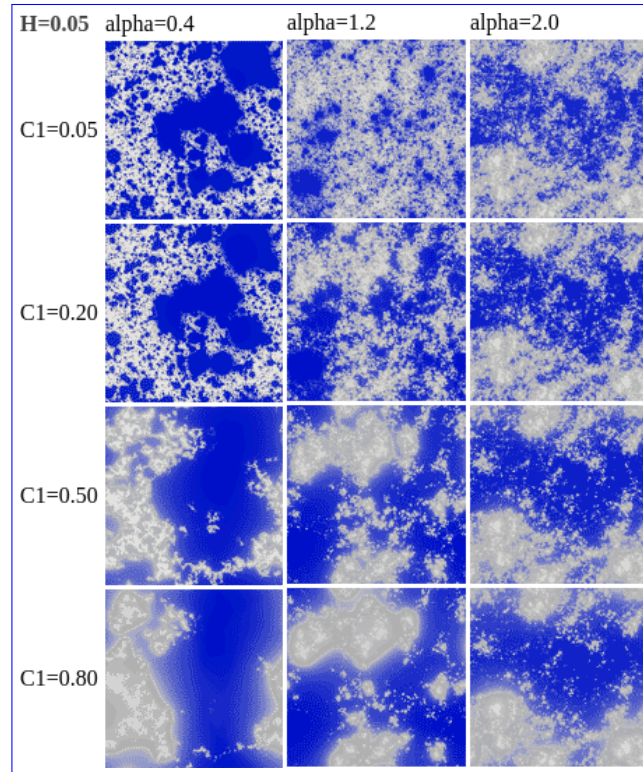

Figure A.1. Illustration of the effect of α and C_1 on randomly generated fields. Blue pixels correspond to zero intensity, whereas pixels with non-zero intensity are shown with a greyscale colormap. Taken from Lovejoy (2017)
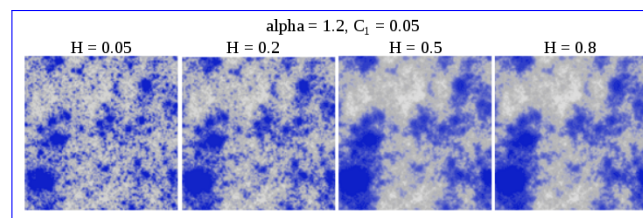

Figure A.2. Illustration of the effect of H on randomly generated fields for $\alpha = 1.2$ and $C_1 = 0.05$. Blue pixels correspond to zero intensity, whereas pixels with non-zero intensity are shown with a greyscale colormap. Taken from Lovejoy (2017)
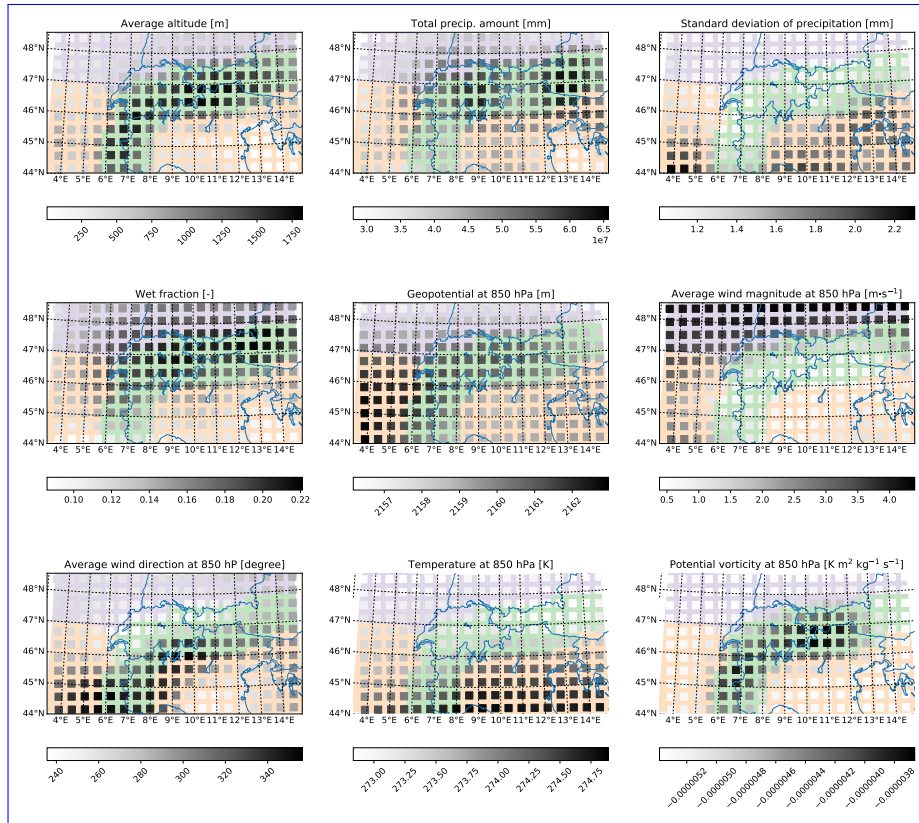
Figure B.3. Spatial representation of the location of all areas used in the climatological study of multifractal parameters as well as the corresponding local descriptors. Note that the squares are mere indicators of the location of the center of all areas and their size is not in scale with their real sizes. The colors drawn below the squares correspond to the classification detailed in Section 4.2.